MASS OUTFLOW FROM RED GIANT STARS IN M13, M15, AND M92

Sz. Mészáros[1,3], E. H. Avrett[2,4], and A. K. Dupree[2,5]

ABSTRACT

Chromospheric model calculations of the Hα line for selected red giant branch (RGB) and asymptotic giant branch (AGB) stars in the globular clusters M13, M15, and M92 are constructed to derive mass loss rates. The model spectra are compared to the observations obtained with the Hectochelle on the MMT telescope. These stars show strong Hα emissions and blue-shifted Hα cores signaling that mass outflow is present in all stars. Outflow velocities of 3−19 km s^{-1}, larger than indicated by Hα profiles, are needed in the upper chromosphere to achieve good agreement between the model spectra and the observations. The resulting mass loss rates range from 0.6×10^{-9} to 5×10^{-9} M$_\odot$ yr^{-1}, which are about an order of magnitude lower than predicted from "Reimers' law" or inferred from the infrared excess of similar stars. The mass loss rate increases slightly with luminosity and with decreasing effective temperature. Stars in the more metal-rich M13 have higher mass loss rates by a factor of ∼2 than in the metal-poor clusters M15 and M92. A fit to the mass loss rates is given by: $\dot{M}[\mathrm{M}_\odot\ \mathrm{yr}^{-1}] = 0.092 \times \mathrm{L}^{0.16}\times \mathrm{T}_{\mathrm{eff}}^{-2.02}\times\mathrm{A}^{0.37}$ where $\mathrm{A}=10^{[Fe/H]}$. Multiple observations of stars revealed one object in M15, K757, in which the mass outflow increased by a factor of 6 between two observations separated by 18 months. Other stars showed changes in mass loss rate by a factor of 1.5 or less.

Subject headings: stars: chromospheres – stars: mass loss – stars: AGB and post-AGB – globular clusters: general – globular clusters: individual (M13, M15, M92)

1. Introduction

Stellar evolution theory predicts that low-mass Population II stars ascending the red giant branch (RGB) for the first time must lose mass (Renzini 1981; Sweigart et al. 1990). Iben & Rood (1970) conjectured that mass loss on the RGB may increase with metallicity in order to account for

[1]Department of Optics and Quantum Electronics, University of Szeged, 6701 Szeged, Hungary

[2]Harvard-Smithsonian Center for Astrophysics, Cambridge, MA 02138

[3]e-mail address: meszi@physx.u-szeged.hu

[4]e-mail address: eavrett@cfa.harvard.edu

[5]e-mail address: dupree@cfa.harvard.edu

colors on the horizontal branch. Direct observations of the ongoing mass loss process in globular clusters only became possible in the past decade using high resolution spectroscopy and infrared imaging from space. For stellar evolution calculations, the mass loss rate from late-type giants is frequently described by "Reimers' law" (Reimers 1975, 1977) given as $\dot{M}[M_{\odot}yr^{-1}] = \eta \times L_* \times R_*/M_*$, where L_*, R_*, and M_* are the stellar luminosity, radius, and mass in solar units, and η is a fitting parameter equal to 4×10^{-13}. This approximation is based on a handful of luminous Population I stars. Schröder & Cuntz (2005) offered another semi-empirical relation for the mass loss rate from cool stars by assuming a wave-driven wind and introducing gravity and effective temperature into the formulation. They found consistency with calculations of evolutionary models for abundances as low as [Fe/H]=−1.27 although metallicity does not enter as a parameter in their formulation.

Origlia et al. (2007) identified dusty RGB stars in 47 Tuc from *Spitzer* mid-IR photometry and derived an empirical (dust) mass loss law for these stars. Mass loss rates derived from their observations suggested that the mass loss increases with luminosity, and is episodic since an infrared excess is not found in all stars. Boyer et al. (2006) also detected a population of dusty red giants near the center of M15. The similarities in Hα line profile characteristics between the *Spitzer* sources and other red giants in M15 suggests the IR emission attributed to circumstellar dust must be produced by an episodic process (Mészáros et al. 2008). Boyer et al. (2008) observed dust production possibly associated with 3 AGB stars in ω Cen with *Spitzer*. They estimated a high mass loss rate for these AGB stars of $2.9{-}4.2{\times}10^{-7}$ $M_{\odot}$ yr^{-1}; however, normal RGB stars in ω Cen do not appear to show strong mass loss as evidenced by the presence of dust.

Indirect evidence of mass loss processes would be the detection of an intracluster medium. Ionized intracluster gas was found in 47 Tucanae by measuring the radio dispersion of millisecond pulsars in the cluster (Freire et al. 2001), while intracluster dust in M15 was first identified by Evans et al. (2003). None of the detections reveal the amount of intracluster material expected from the cluster giants (Barmby et al. 2009; Matsunaga et al. 2008).

Stars in several clusters have been examined with high resolution spectroscopy to search for signs of mass loss in their Hα and Ca II K profiles. A detailed study carried out by Cacciari et al. (2004) included 137 red giant stars in NGC 2808. Most of the stars brighter than log $(L/L_{\odot}) = 2.5$ showed emission wings in Hα. The velocity shift of the Hα line core relative to the photosphere was less than ≈ -9 km s^{-1}. Mészáros et al. (2008, 2009) also found velocity shifts in the Hα absorption line in M13, M15 and M92 down to a limiting luminosity of log $(L/L_{\odot}) = 2.0$. The line bisector showed increasing outflow velocities in the Hα core up to $7{-}10$ km s^{-1} above log $(L/L_{\odot}) \sim 2.5$. The Ca II K line suggested higher velocities and an accelerating outflow. The outflow velocities appear to be independent of cluster metallicity.

In order to evaluate the mass flow, detailed non-LTE modeling with semi-empirical atmospheres is necessary to reproduce the optical line profiles and infer the mass loss rates from the stars. Such non-LTE modeling was first carried out by Dupree et al. (1984). They showed that the emission

wings of the Hα line found in metal-deficient giant stars can arise naturally from an extended, static chromosphere, and emission asymmetry and shifts in the Hα core indicate mass loss. Spherical models with expanding atmospheres suggested the mass loss rates are less than 2×10^{-9} $M_\odot$ yr^{-1} a value which is less than predicted by the Reimer's relationship. McDonald & van Loon (2007) calculated mass loss rates of two stars in M15 by modeling the Hα and Ca II K lines with simple LTE approximations. They found mass loss rates of several times 10^{-8} and $10^{-7}M_\odot$ yr^{-1}, but the use of LTE models for a chromosphere can not be considered reliable. Mauas et al. (2006) computed semi-empirical Hα and Ca II K profiles for 5 RGB stars in NGC 2808 including non-LTE effects in spherical coordinates. Their line profiles fit the observations when an outward velocity field is included in the model chromosphere, in agreement with previous calculations (Dupree et al. 1984). The derived mass loss rates exhibited a large range around 10^{-9} $M_\odot$ yr^{-1}. Outflow velocities from 10 km s^{-1} up to 80 km s^{-1} were needed by Mauas et al. (2006) in order to match the observed line profiles. Lyons et al. (1996) discussed the Hα and Na I D line profiles for RGB stars in M4, M13, M22, M55, and ω Cen. The core shifts were less than 10 km s^{-1}, much smaller than the escape velocity from the stellar atmosphere at 2 R_* ($\approx 50 - 70$ km s^{-1}). Dupree et al. (1994) observed 2 RGB stars in NGC 6752 and found that the Ca II K and Hα core shifts were also low, less than 10 km s^{-1}. However, asymmetries in the Mg II lines showed strong outflow velocities (≈ 150 km s^{-1}) in cluster giants and metal-poor field stars (Dupree et al. 1994, 2007; Smith & Dupree 1998). Also, high outflow velocities, (30−140 km s^{-1}), were found in the He I λ10830 absorption line of metal-poor red giant stars of which 6 are in M13 (Dupree et al. 1992; Smith et al. 2004; Dupree et al. 2009). Mg II lines and He I λ10830 are formed higher in the atmosphere than Hα and Ca II K, which suggests that the stellar wind becomes detectable near the top of the chromosphere. These outflow velocities are frequently higher than the central escape velocities from globular clusters, namely 20−70 km s^{-1} (McLaughlin & van der Marel 2005).

In this paper, we select a sample of giant stars to model whose spectra have been obtained previously with Hectochelle (Mészáros et al. 2008, 2009). They span a factor of 5 in metallicity (from [Fe/H]=−1.54 to −2.28) and a factor of 6 in luminosity [from log ($L/L_\odot$) =2.57 to 3.38]. Five stars have been observed more than once. Characteristics of the selected targets are described in Section 2. Section 3 contains the details of the non-LTE models in both the static and expanding versions. Section 4 compares the calculations with Hα line profiles, and the construction of a mass loss relation and its dependence on temperature, luminosity, and abundance. Our Conclusions can be found in Section 5.

2. Target Stars

Observations of Hα in a total of 297 red giant stars in M13, M15, and M92 were obtained in 2005 May, 2006 May, and 2006 October with the Hectochelle on the MMT (Mészáros et al. 2008, 2009) with a spectral resolution of about 34,000. To investigate the dependence of the mass loss rate on luminosity, temperature, and metallicity, we chose RGB stars from each cluster that had

clear Hα emission and a range of at least a factor of two in luminosity. The sample of stars includes different intensity ratios of the Hα emission wings, B/R[1], and the bisector velocities varied ($v_{\rm bis}$) from -0.7 to -8.9 km s^{-1}. To monitor the mass loss changes in time, one star in M13 (L72), one in M92 (VII-18), and three stars in M15 (K341, K757, and K969) were selected which have multiple observations. One star without Hα emission was also selected from each cluster to extend the sample to lower luminosities and higher temperatures. Our previous study of M15 (Mészáros et al. 2008) found no signature of different outflows or chromospheric structure between the 'dusty' stars identified by the *Spitzer* Space Telescope (Boyer et al. 2006) and normal RGB objects. Modeling of the Hα profile could reveal dynamical differences, if present. Two AGB stars in M15 with excess dust (K421, K479) were selected for modeling to investigate whether the mass loss of these stars differs from the rest. The color magnitude diagram (CMD) of the cluster members and targets for modeling can be seen in Figure 1; target stars are listed in Table 1.

A total of 15 stars was selected including from 4 to 6 in each of the 3 globular clusters; five stars had multiple spectra so that we could estimate changes in the mass loss rate from the Hα profiles. Unreddened colors for M13, M15, and M92 stars were calculated using the foreground reddening and the apparent distance modulus from the catalog of Harris (1996). The effective temperatures, bolometric corrections, and luminosities were obtained from the V$-$K colors using the empirical calibrations by Alonso et al. (1999, 2001) and the cluster average metallicity (Harris 1996) [Fe/H]$=-1.54$ for M13, [Fe/H]$=-2.26$ for M15, [Fe/H]$=-2.28$ for M92 [see Mészáros et al. (2008, 2009) for more details].

3. The Models

Our technique consists of constructing a static photosphere and chromosphere model and then changing the temperature at each depth until the Hα profile depth, width, and emission strength and asymmetries are roughly consistent with observed profiles. At this point, the model atmosphere and profile are calculated in spherical symmetry with an assumed velocity field, and then iterated to match the observed profiles. We discuss each of these procedures in turn.

3.1. Static Chromosphere

Two separate photospheric models were calculated with ATLAS (Kurucz 1993), one for stars in M13 and one for stars in M15 and M92. In order to create the initial photospheric models, we used log g=0.45, [Fe/H]$=-2.45$, T=4275K for the metal poor stars, and log g=0.5, [Fe/H]$=-1.5$, T=4500K for the metal rich stars. Although the photospheric parameters of the target stars are different, this does not affect the calculated line profiles, because the Hα line forms in the

[1]B signifies the short-wavelength emission peak and R the long-wavelength emission peak.

extended warm chromosphere. The model atmospheres were represented by 72 depths, where the photospheric distribution was given by the original Kurucz values at the innermost 12 points. For the emission line calculations, we changed the parameters at the outer depths to represent a chromosphere with the temperature increasing linearly with decreasing mass column density [ZMASS (g cm^{-2})]. Examples of these chromosphere can be seen in Figure 2 (*upper panels*) as a function of depth index. In every model we assumed the stellar radius to be equal to $70R_{\odot}$ and a microturbulent velocity of 4 km s^{-1} at each point of the atmosphere. We assumed that every star has a mass of 0.8 $M_{\odot}$, making the gravity, g, also a constant parameter. This way the models depend on three free parameters: 1) the column mass and temperature where the chromosphere starts; 2) the slope of the T−ZMASS function; 3) the highest temperature (T_{max}) and the lowest ZMASS values of the chromosphere, where the transition region starts. For further simplicity, the column mass and temperature where the chromosphere starts, and the mass column density where the chromosphere stops were also fixed. A transition region with a maximum temperature 2×10^5K was added to every model in the last 10 points to obtain small optical depths as hydrogen becomes completely ionized. The chromosphere was represented at 50 points linearly distributed in T vs. log ZMASS, which was sufficient to sample in detail the region where the Hα wings and core form.

For every T−ZMASS distribution, we solved the non-LTE radiative transfer and the statistical and hydrostatic equilibrium equations, using the program PANDORA (Avrett & Loeser 2003). By keeping the starting T-ZMASS point, and the ending ZMASS point of the chromosphere the same, the only control parameter of the input models was the T_{max} value, which established the slope of the T−ZMASS distribution. This parametrization allowed us to handle easily many different input models for the PANDORA program. These chromospheric models can be seen in Figure 3, and they are listed in Table 2. We computed the non−LTE populations of a 15−level hydrogen atom assuming the same value of the gravity, g, and [Fe/H] used in the photospheric models. All heavy elements were scaled using the metallicity used in the photospheric models and assuming the solar abundance distribution. For the continuum calculations we included all 15 bound-free transitions, and the most important bound-bound transitions and scattering that contribute to the photoionization of hydrogen. In every model we assumed a microturbulent velocity of 4 km s^{-1} in each point of the atmosphere.

Calculations were carried out in two phases for all models: in the first phase a plane-parallel approximation was used in order to calculate the scale of the atmosphere and the total H density from the initial and fixed ZMASS values, the Kurucz scale height, and total H density. A run was considered converged if the new height scale and total H density did not change by more than 1% as compared to the previous run. After this, the plane-parallel atmosphere was replaced with a spherical atmosphere with the same stratification, and this spherical model was used to calculate the emergent spectrum. To check the accuracy of our input approximations, we changed the input radius, gravity, and [Fe/H] each by a factor of 2 for one model. Changing the [Fe/H] does not affect the line profiles, but the radius and gravity do. A smaller radius (and larger gravity) leads to stronger emission. Although the line profile changes, the changes in radius and gravity do not

affect the derived mass loss rates by more than our errors from the velocity-field determination (see next section).

3.2. Expanding Atmosphere

From Figure 3, one can see that emission wings arise in warm, static chromospheres. However, the static atmosphere cannot explain the asymmetry of the emission wings and the 'banana-shaped' bisector of the observed profiles (Dupree et al. 1984). Thus, flow velocities must be present in the atmosphere. Accordingly, the regions where the core and wings of the Hα line are formed were put in motion. We constructed velocity distributions in order to produce asymmetrical line profiles to match the observed line asymmetries. This velocity field is included when calculating the line source function. The line-forming regions were determined from the depths where the maximum contributions to the spectrum occur. The Hα line core forms between depths 16−21 (8000−9900 K), the wings from between depths 24−35 (5800−7800 K) in every model, depending on T_{max}. The rest of the atmosphere does not affect the line profile, thus we do not have information on the velocity field outside these regions. The velocity was changed usually between −14 and 20 km s^{-1}, where the negative number means an inward velocity and the positive number means an outward velocity relative to the photosphere.

In order to match the line profiles, three characteristics of Hα were considered: 1) the bisector velocity (v_{bis}) and the position of the Hα core, 2) the width of the Hα absorption line, and 3) the ratio of of the strength of the blue and red emission wings (B/R). The velocities of v_{bis} are calculated in the following way (Mészáros et al. 2008): the absorption line is divided into about 20 sectors of equivalent depth; the top and the lower 3 sectors are selected and the wavelength average of the top and lower sectors is calculated, subtracted one from another and changed to a velocity scale. The fitting was done by, first, taking a well converged spherical run in which the modeled emission matched the observation. The strength of the emission has an important effect on the calculated mass loss rate, because in our approximations it scales the atmosphere. Higher T_{max} corresponds to a larger height scale (Figure 2, lower panels), and smaller hydrogen density, because the mass column density is the same in every model. Then, the previously measured bisector velocity of the Hα absorption line gave an estimate of the expanding velocity in the core. However, in almost every case this velocity did not yield the same bisector and position of the core in the calculated profile as in the observed one. Higher values of the velocities were required indicating that the measured Hα bisectors are a lower limit to the actual velocity fields present in the star. Nearly a factor of 2 higher velocities were necessary in the models in every case. The value of velocity in the region where the wings form influences the B/R ratio. In most cases, if B/R>1, then an inward velocity was needed; when B/R<1, an outflowing velocity was required. Our observations show that the Hα line cores are either at rest or moving outward from the star. Moreover, the line asymmetries can change from one observation to another, thus a complex time-dependent velocity field must be present in these chromospheres.

The microturbulent velocity was also changed from 4 km s^{-1} (used in the generic spherical calculations) in order to match the width along the Hα line with the observation. The assigned microturbulent velocity varied between 6 and 14 km s^{-1} in the region where the wings of the Hα line form, and 0 km s^{-1} where the core forms in order to better match the width of the core. After the calculation was completed, the model profile was compared with the observation by eye and further adjustments were made to the velocity field. This was continued until the modeled and observed line profiles matched each other as well as possible. The mass loss was then estimated with a simple formula based on mass outflow:

$$\dot{M}(\mathrm{M}_{\odot}\ \mathrm{yr}^{-1}) = 2.33 \times 10^{-26} \times \mathrm{m}_H \times \mathrm{N}_H \times 4\ \pi \times \mathrm{R}^2 \times \mathrm{V}_{exp}$$

where m_H(g) is the mass of the hydrogen atom, N_H(cm^{-3}) is the total hydrogen density, R(cm) is the distance from stellar center, and $V_{\rm exp}$(cm s^{-1}) is the velocity of the outermost layer. In our calculation the velocity, distance, and hydrogen density of the outermost layer forming the line core gave the mass loss rate for each star.

To obtain an estimate of the error of the mass loss rates, the expanding velocity in the wing and core forming regions was changed by $\pm$1 km s^{-1} in every depth. In both cases the mass loss changes by less than a factor of 2 and the line profile changes are not visible by eye. Changing every depth by $\pm$2 km s^{-1} usually gave a worse fit to the observation; thus we conclude that the error in the derived mass loss rates appears to be a factor of 2.

4. Discussion

4.1. Observed and Calculated Profiles

The comparison of observed and calculated spectra is shown in Figures 4−9, and the derived mass loss rates are listed in Table 2. The spectra were computed at high resolution, and were convoluted with a Gaussian distribution corresponding to the spectral resolution of ∼34000. We aim to match several of the line parameters: the central core depth, the core velocity shift, the line width, the strength and the asymmetry of the emission wings. Changing the model usually produces changes in more than one line parameter, and so our final model, the 'best fit', is frequently a compromise solution. In some cases the continuum level of the observed spectrum was shifted to match the calculated one, and we were able to match the observed profiles fairly well. The main difference between calculations and observations is that the computed Hα profiles are slightly broader and deeper in the core; similar systematic differences were found by Mauas et al. (2006). This suggests that in our models there is either slightly more hydrogen in the atmosphere where the Hα core forms, or the chromosphere is hotter, thus increasing scattering from the core. The calculated atmospheres are homogeneous in every case, so that the difference in the core might also come from inhomogeneities in the atmosphere. This, however, does not affect the mass loss rate calculations by more than a factor of 2, because the wing asymmetry, bisector, and the position of

the core are taken into account in fitting the observed profiles, and these characteristics are more important in determining the calculated mass loss. This homogeneous chromosphere approximation gives better results for brighter objects (for example L973 in M13, Figure 4) and only the faintest stars in each cluster (L592 in M13, K87 in M15 and XII-34 in M92) show major differences in the Hα core. In some cases an inward velocity had to be used where the emission wings formed in order to match the wing asymmetry, but in all cases an outward velocity was necessary to fit the core.

The stars, L592, K87, and XII-34 did not show any emission in Hα and have lower luminosities than other selected RGB stars with Hα emission. This makes it difficult to derive a mass loss rate for these stars. It was not possible to construct an accurate model when emission is not visible in the spectrum, because in our approach the emission wings were used to give the slope of the temperature versus mass column density in the static chromosphere. Thus only the bisector and the core of the Hα line affect the fit. The difference between the observed and calculated profile also derives from the fact that the radius and surface gravity for these stars are quite different (much smaller) than we assumed in each calculation. In order to check the accuracy of the derived mass loss rate, a static, spherical chromosphere was calculated using R=35R$_\odot$ and log g=1.25 −− parameters close to the values for these stars. The same velocity field was applied to this chromosphere as to the others. The mass loss rates do not differ from each other by more than a factor of 2, but the new profiles using the smaller radius do not match the observations very well. Thus, in the final interpretation here we use the model with R=70R$_\odot$.

The Hα core generally forms between T=8000 and 9900K, which, in our models, is located between 1.4 and 2.0 R$_*$ in the chromosphere. All of the observed Hα profiles have a static or outflowing core. The semi-empirical models thus all require outflow at the top of the atmosphere in order to match the profiles. At the highest temperatures ($T > 10^4$K), there is no contribution to the Hα profile, hence we have no information on any velocity field that might be present. Thus, we have reduced the velocity to zero. At lower levels in the atmosphere, below T$\sim$8000K either inflow or outflow occurs. The direction of the velocity field in the model is determined by the asymmetry of the line wing emission. When B<R, an outflowing velocity is required; when B>R, an inflowing velocity is required.

Outflowing velocities used in the modeling vary between 3 and 19 km s^{-1}, which are much smaller than the escape velocity (50−70 km s^{-1}) from this part of the chromosphere (Table 2). In our spectra, the Hα core is either at zero velocity with respect to the star, or moving outwards. There are no signs of any inflow in the core itself. Therefore it appears reasonable to assume that the outward velocity continues to increase until the escape velocity is reached. While the material is not escaping from the chromosphere where the Hα core forms, analysis of Mg II lines and the He I λ10830 absorption line of RGB stars in NGC 6752, M13, and metal-poor field giants shows that velocities can reach up to 140 km s^{-1} (Dupree et al. 1992, 1994, 2007, 2009; Smith et al. 2004). These lines are formed higher in the atmosphere than Hα, which suggests that the mechanisms driving the stellar winds become stronger above the top of the chromosphere and escape of material is only possible at distances >2.0 R$_*$.

4.2. Changes in Time

One star in M13 (L72) and M92 (VII-18) and three stars in M15 (K341, K757, and K969) were observed more than once, which allows us to examine how the mass loss might change between observations. Separate semi-empirical atmospheric models were constructed to match each of the observed profiles. Of these 5 stars, three showed evidence of a difference in the mass loss rate, and two had nearly the same mass loss rate between observations. In the case of K341 (Figure 6) the mass loss rate changed only slightly with the respect to the observed spectrum, and these differences are smaller than the error of the mass loss determination. L72 showed less than a factor of 2 change in the mass loss rate over a month time span even though the observed spectra are quite different in the asymmetry of the emission wings (Figure 4). Although the atmospheric motions changed, this created only a slight difference in the mass loss rate. A much larger difference occurred in K757 (Figure 7), where the core asymmetry became prominent, and the derived mass loss rate increased from 5.7×10^{-10} $M_\odot$ yr^{-1} to 3.0×10^{-9} $M_\odot$ yr^{-1} – by almost a factor of 6. Nearly one and a half years separate these two observations. Such large changes were visible in AGB stars in M15 (Mészáros et al. 2008) near $\log(L/L_\odot) \sim 2.0 - 2.7$ in 1.5 years. This star, K757, is however on the RGB according to its position on the CMD (Figure 1) and was not identified as a dusty AGB star by Boyer et al. (2006), which demonstrates that large changes in the mass loss rate can occur on the RGB as well.

Of these 5 stars, two showed evidence of pulsation in the spectra. The B/R ratio of emission in the spectra of K341 changed between observations. During the first observation (2005 May) the emission asymmetry signals inflow; in the following 3 observations (2006 May and October) the asymmetry suggests different values of outflow. Although in the case of the first observation the modeled velocity is slightly greater than zero, the emission ratio cannot be modeled with outflow velocities. The Hα core, however, shows an outflow in every observation. We take this as evidence of a pulsation present in the lower chromosphere. Our models show that the pulsation extends outwards into the chromosphere to around 1.4−1.5 R_*; at these levels and below, both inward and outward flows are possible, but the higher parts of the chromosphere (>1.5 R_*) do not participate in the pulsation. It is more likely that pulsation itself helps to drive the mass outflow. The only other star with varying inflow and outflow velocities where the emission forms is K969. The dust-free models of Struck et al. (2004) suggest that a stellar wind may be supported by shock waves which travel through the wind, possibly related to the pulsation in the lower levels of the atmosphere, similar to what is present here in the red giants.

4.3. Dependence on Luminosity, Effective Temperature and Metallicity

Although the bisector velocity was one of the key parameters taken into account while fitting the models to the observations, the relation between the bisector velocity and the derived mass loss rate is not unambiguous. Generally the semi-empirical models require higher expansion velocities

than the measured bisector velocity. In some cases, matching a spectrum exhibiting a low bisector velocity (< -2 km s^{-1}) is only possible with models assuming high outflow velocities (>10 km s^{-1}) in the core. This usually occurs when either the blue or the red emission is weak. Also, while calculating the bisectors of the line profiles, the top sector was close to the continuum in the normalized spectrum, but the lowest sector was placed $0.01 - 0.05$ above the lowest value of the line depending on the signal-to-noise ratio in the line core. In these cases, matching the position of the core was significant in the fitting, which was only possible using high outflowing velocities (>10 km s^{-1}).

The mass loss rate weakly increases with luminosity and with decreasing effective temperature in M15 and M92 (Figure 10). This is because the bisector velocity increases with luminosity (decreases with effective temperature), and while the atmospheres of these stars are larger and thus less dense, the increase in expansion velocity necessary to reproduce the absorption line profile gives an overall higher mass outflow. This weak dependence is affected by the error of modeling and the changes with time in the dynamics of the atmosphere. It is also evident that stars in the more metal rich cluster, M13, have larger mass loss rates than in the metal poor clusters M15 and M92, although this difference is close to our errors. This is expected from the previously observed bisector velocity−luminosity relation (Mészáros et al. 2008, 2009), because the Hα line bisector velocity was one of the key fitting parameters. In M13, low (close to -2 km s^{-1}) bisector velocities were measured for the most luminous stars (L954, L973, log $(L/L_{\odot}) > 3.3$, Figure 4) from Hα and because bisector velocity was a significant fitting parameter, the derived mass loss rates are comparable to those for the fainter stars. Although the bisector velocities of the Hα core approach -2 km s^{-1} as compared to -6 to -9 km s^{-1} for stars between log $(L/L_{\odot}) = 3.0$ and 3.3, the mass loss rate did not decrease significantly. Our spectra showed (Mészáros et al. 2009) that the velocities as determined from the Hα profile decrease at the highest luminosity which may result from the changing atmospheric structure in the most luminous stars. It does not seem physically reasonable that the outflow would cease at the highest luminosities. The mass loss rate did not change greatly for these objects, because relatively high velocities are needed to use to match the position of the core in the Hα line. In sum, the values of the rates that we find are generally similar to the non-LTE studies of Hα in other metal-poor giants (Dupree et al. 1984; Mauas et al. 2006).

4.4. Comparison with Other Models and Mass Loss Relations

The values of the mass loss rates that we find range from 0.6×10^{-9} to 5×10^{-9} ($M_{\odot}$ yr^{-1}). These values are in general agreement with other calculations for metal-deficient giant stars in the field or in the cluster NGC 2808. Mauas et al. (2006) modeled five very cool stars (T_{eff} <4015K) and found differences in the mass loss rates amounting to a factor of 38 – with values ranging from 0.1×10^{-9} to 3.8×10^{-9} $M_{\odot}$ yr^{-1}. This may reflect the sort of episodic change that might lead to dust production. However, because the line cores of Hα in the models do not seem to well match the observed profiles, the derived mass loss rates could be affected. Their velocity profiles also differ

from ours. In fact, inward velocities were not required to match the observed Hα emission line profiles, even if they signaled inflow. For line profiles with B>R, they introduced a decelerating velocity field with increasing radius in order to match the profiles. Thus, the zero point of the chromospheric velocity is different.

The literature contains various relationships to estimate the mass loss rates for luminous cool stars. The widely used 'Reimers law' based on dimensional arguments (Reimers 1975, 1977), derives from a handful of Population I giant stars. This mass loss formula was later revisited by Catelan (2000) and suggested a stronger dependence on luminosity, radius and log g. The SC relationship (Schröder & Cuntz 2005) is more detailed and includes gravity and effective temperature and assumes that the wind arises from an extended, highly turbulent chromosphere, possibly associated with Alfven waves. They did not consider extremely metal-deficient stars, such as those in M15, in their calibration. Origlia et al. (2007) presented an empirical (dusty) mass loss formula based the globular cluster 47 Tuc. Dusty RGB stars were identified from mid-IR photometry with *Spitzer*. Mass loss rates were calculated by modeling the emerging spectrum and dust emission with the DUSTY code (Ivezić et al. 1999; Elitzur & Ivezić 2001). The dependence of the mass loss rate on luminosity is much shallower than suggested by the Reimers relationship.

These rates are shown in Figure 10 and listed in Table 3, where they differ from our model calculations by an order of magnitude at least. For the faintest stars, below log $(L/L_{\odot}) = 2.8$ the Schröder-Cuntz (SC) relation predicts the lowest values of the 3 approximations; at higher luminosities the difference between the SC relation and our model calculations increases, amounting to an order of magnitude at the highest luminosities. While the slope of the Origlia relationship with luminosity is similar to ours, the predicted values of the mass loss rate are larger by more than an order of magnitude. Their formulation included a scaling factor, C, which is the product of the gas-to-dust ratio, the expansion velocity, and the grain density. They set $C = 1$ for 47 Tuc. Our clusters are lower in metallicity, presumably increasing the gas:dust ratio and the expansion velocities are slightly higher than the 10 km s^{-1} taken by Origlia et al. (2007). Thus, for the same grain density, the discrepancy between the dust rates and the modeled Hα rates would increase.

The rates derived for dusty winds from mid-IR photometry are consistently higher than those indicated by the gas. If the dust is produced episodically (Mészáros et al. 2008; Origlia et al. 2007) at these high rates, it is puzzling that anomalously massive outflows have not been detected in the optical spectra. The IR observations led Origlia et al. (2007) to conclude that mass loss in 47 Tuc is ongoing in a fraction of the stars ranging from 16 to 32 percent on the RGB, whereas the Hα spectra and modeling of stars in M13, M15, and M92 shows that all of the stars have outflowing chromospheric material.

Models of two stars in M15, K421 and K479, previously identified as dusty AGB stars by Boyer et al. (2006) were also calculated (Figure 9). These stars are similar in luminosity, effective temperature, and bisector velocity to other RGB stars included. For these two stars we find no difference in mass loss rate from other red giants. Mass loss rates suggested by the IR excess exceed

by more than an order of magnitude the rates inferred from H-alpha. If the mass loss must be high in order to produce dust, we conclude that the M15 giants are not currently undergoing an episode of dust-production. The dust observed in the dusty RGB stars most likely left the star decades earlier so one does not necessarily expect a correlation between time varying chromospheric phenomena and dusty envelopes.

A least-squares fit to our mass loss rates as a function of luminosity, temperature and [Fe/H] yields the following form:

$$\dot{M}[\mathrm{M}_\odot\ \mathrm{yr}^{-1}] = 0.092\ \times\ \mathrm{L}^{0.16}\times\ \mathrm{T}_{\mathrm{eff}}^{-2.02}\times\mathrm{A}^{0.37}\ \text{where A=}10^{[Fe/H]}.$$

Here we have excluded the 2 most luminous stars of M13 from the fit, because we believe that Hα becomes less sensitive to the mass outflow at the low temperatures of the metal-rich red giants. The values calculated from this relationship are given in Table 3 and shown in Figure 10.

5. Conclusions

1. Chromospheric modeling of the H-alpha line in several clusters demonstrates that the mass loss rate increases with increasing luminosity and decreasing effective temperature of stars on the red giant branch. All stars modeled down to 2 magnitudes below the RGB tip show outflowing material suggesting that mass loss is a continuous process. The more metal-rich stars have a higher mass loss rate than the metal-poor stars. We offer a new relationship for mass loss rates in Pop II stars based on these models.

2. The calculated mass loss rates from the Hα profile give values that are an order of magnitude less than those estimated from the Reimers (1975, 1977), SC (Schröder & Cuntz 2005), and Origlia et al. (2007) relationships. Differences are larger at higher luminosities. The Hα mass loss rates and the Origlia relationship give a very similar shallow dependence on luminosity.

3. At the top of the RGB, for stars brighter than log $(L/L_\odot) = 3.3$, the Hα line may not be adequately sensitive to the mass loss rate; the models suggest lower mass loss rates for these objects.

4. An expanding velocity at the top of the atmosphere was required for every star in order to match the Hα core. The largest outflowing velocity reached 19 km s^{-1}, usually larger by factors up to 10 than indicated by the bisector velocity. In the region where the Hα emission is formed, the velocities can change direction, indicating the presence of pulsation.

5. Two stars previously identified as dusty red giant stars in M15 show no difference in mass loss rate from other red giants. If high rates of mass loss are needed in order to produce dust, we conclude that the M15 giants are not currently undergoing an episode of dust-production.

6. K757 (M15) shows a factor of 6 mass loss−rate change in a time span of 18 months (from

5.7×10^{-10} $M_\odot$ yr^{-1} to 3.0×10^{-9} $M_\odot$ yr^{-1}). A smaller change occurred in two other stars, K341 (M15) and L72 (M13), where the mass loss difference was nearly a factor of 2.

We are grateful to Rudi Loeser who was instrumental in developing the PANDORA code. We thank Bob Kurucz for help with the model photospheres. Szabolcs Meszaros is supported in part by a SAO Predoctoral Fellowship, NASA, and the Hungarian OTKA Grant K76816. This research is also supported in part by the Smithsonian Astrophysical Observatory.

REFERENCES

Alonso, A., Arribas, S., & Martínez-Roger, C. 1999, A&AS, 140, 261

Alonso, A., Arribas, S., & Martínez-Roger, C. 2001, A&A, 376, 1039

Avrett, E. H., & Loeser, R. 2003, in IAU Symp. 210, Modeling of Stellar Atmospheres, ed. W. Weise & N. Piskunov (Dordrecht: Kluwer), A-21

Barmby et al. 2009, AJ, 137, 207

Boyer, M. L., McDonald, I., Loon, J. T., Woodward, C. E., Gehrz, R. D., Evans, A., & Dupree, A. K. 2008, AJ, 135, 1395

Boyer, M. L., Woodward, C. E., van Loon, J. T., Gordon, K. D., Evans, A., Gehrz, R. D., Helton, L. A., & Polomski, E. F. 2006, AJ, 132, 1415

Cacciari, C. et al. 2004, A&A, 413, 343

Catelan, M. 2000, ApJ, 531, 826

Dupree, A. K., Hartmann, L., & Avrett, E. H. 1984, ApJ, 281, L37

Dupree, A. K., Sasselov, D. D., & Lester, J. B. 1992, ApJ, 387, L85

Dupree, A. K., Hartmann, L., Smith, G. H., Rodgers, A. W., Roberts, W. H., & Zucker, D. B. 1994, ApJ, 421, 542

Dupree, A. K., Li, T. Q., & Smith, G. H., 2007, AJ, 134, 1348

Dupree, A. K., Smith, G. H., & Strader, J. 2009, AJ, submitted

Durrell, P. R., & Harris, W. E. 1993, AJ, 105, 1420

Elitzur, M. and Ivezić, Ž. 2001, MNRAS, 327, 403

Evans, A., Stickel, M., van Loon, J. T., Eyres, S. P. S., Hopwood, M. E. L., & Penny, A. J. 2003, A&A, 408, L9

Freire, P. C., Kramer, M., Lyne, A. G., Camilo, F., Manchester, R. N., & D'Amico, N. 2001, ApJ, 557, L105

Harris, W. E. 1996, AJ, 112, 1487

Iben, I., Jr., & Rood, R. T. 1970, ApJ, 161, 587

Ivezić, Ž., Nenkova, M., & Elitzur, M. 1999, User Manual for DUSTY, (Lexington: Univ. Kentucky)

Kurucz, R. L. 1993, in ASPC 44: IAU Colloq. 138: Peculiar versus Normal Phenomena in A-type Related Stars, ed. Dworetsky, M. M., Castelli, F., & Faraggiana, R. (San Francisco: ASP), 87

Kustner, F. 1921, Veroeffentlichungen des Astronomisches Institute der Universitaet Bonn, 15, 1

Ludendorff, H. 1905, Publikationen des Astrophysikalischen Observatoriums zu Potsdam, 50

Lyons, M. A., Kemp, S. N., Bates, B., & Shaw, C. R. 1996, MNRAS, 280, 835

Matsunaga, N. et al. 2008, PASJ, 60, 5415

Mauas, P. J. D., Cacciari, C., & Pasquini, L. 2006, A&A, 454, 609

McDonald, I., & van Loon, J. T. 2007, ApJ, 476, 1261

McLaughlin, D. E., & van der Marel, R. P. 2005, ApJS, 161, 304

Mészáros, Sz., Dupree, A. K., & Szalai, T. 2009, AJ, 137, 4282

Mészáros, Sz., Dupree, A. K., & Szentgyörgyi, A. H. 2008, AJ, 135, 1117

Origlia, L., Rood, R. T., Fabbri, S., Ferraro, F. R., Fusi Pecci, F., & Rich, R. M. 2007, ApJ, 667, L85

Reimers, D. 1975, Mem. Soc. R. Sci Liége, 8, 369

Reimers, D. 1977, A&A, 61, 217

Renzini, A. 1981, in IAU Colloq. 59, Effects of mass loss on Stellar Evolution, ed. C. Chiosi & R. Stalio (Dordrecht: Reidel), 319

Sandage, A. 1970, ApJ, 162, 841

Sandage, A., & Walker, M. F. 1966, ApJ, 143, 313

Schröder, K. P., & Cuntz, M. 2005 ApJ, 630, L73

Smith, G. H., & Dupree, A. K. 1998, AJ, 116, 931

Smith, G. H., Dupree, A. K., & Strader, J. 2004, PASP, 116, 819

Struck, C., Smith, D. C., Willson, L. A., Turner, G., & Bowen, G. H. 2004, MNRAS, 353, 559

Sweigart, A. V., Greggio, L., & Renzini, A. 1990, ApJ, 364, 527

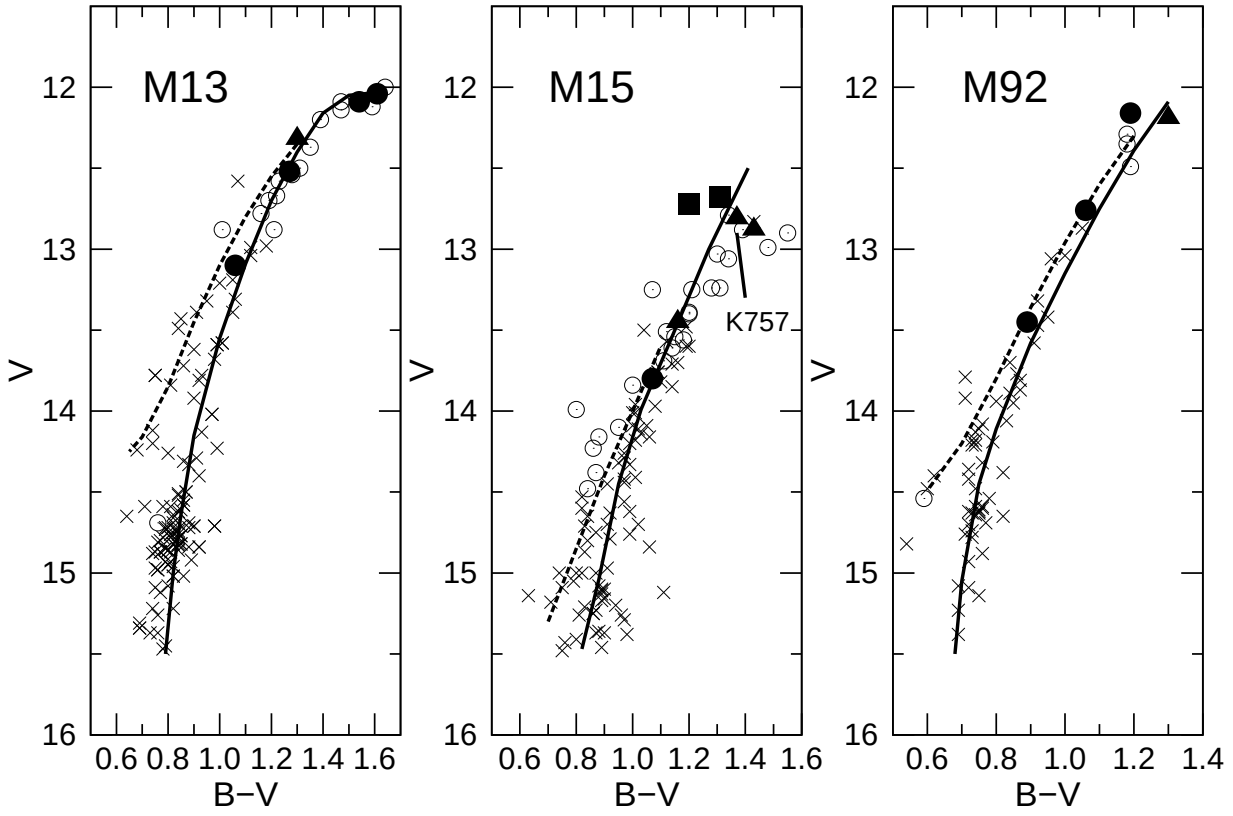

Fig. 1.— Color-magnitude diagram for all stars observed in M13, M15 and M92. Stars with Hα emission are marked by open circles. Filled symbols mark the stars modeled in this paper, where stars observed once are marked by filled circles, stars observed more than once are marked by filled triangles, and stars observed with *Spitzer* (Boyer et al. 2006) are marked by filled squares. The solid line shows the fiducial curve of the RGB; the dashed line traces the fiducial curve of the AGB for M13 and M92 taken from observations of Sandage (1970), and for M15 taken from observations of Durrell & Harris (1993).

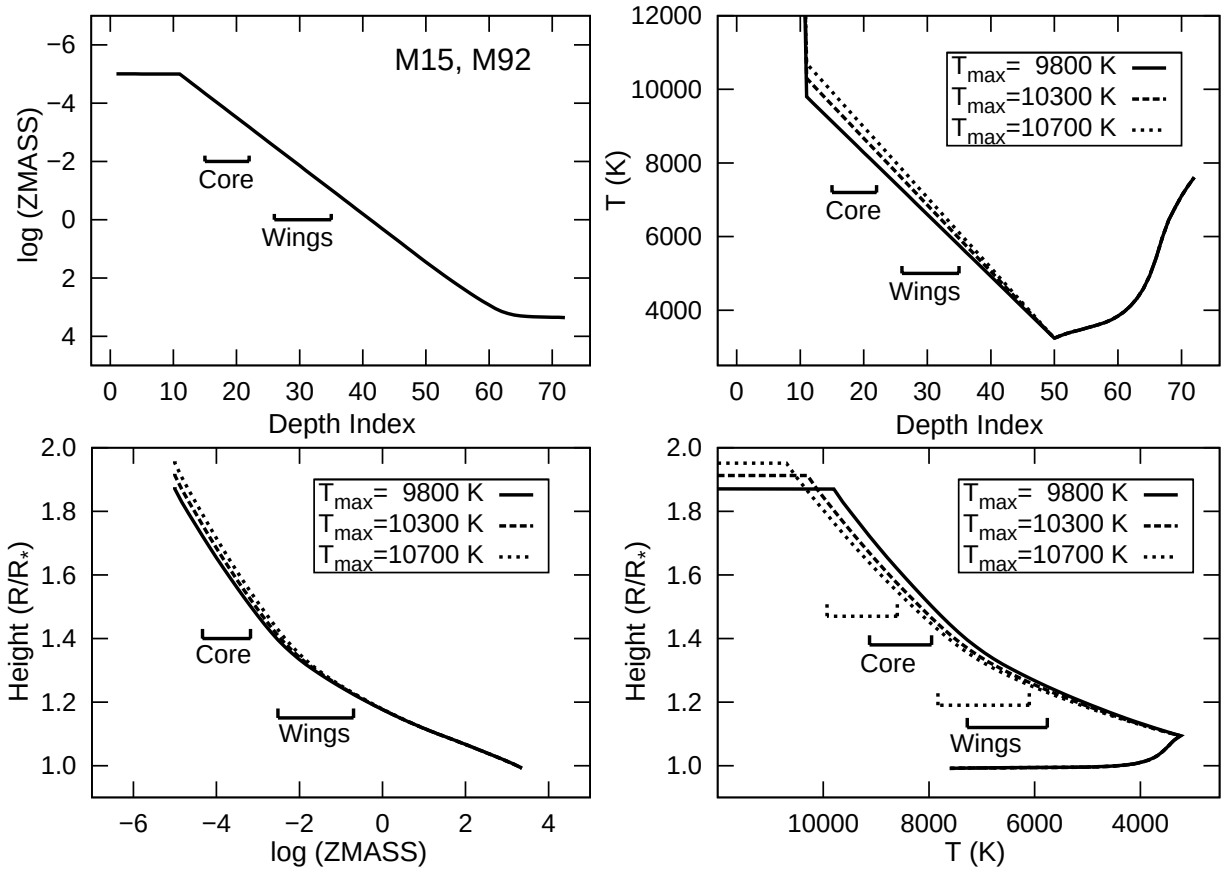

Fig. 2.— *Top left and right:* The mass column density and temperature of three selected input models as a function of depth index. The atmosphere was sampled with 72 points, the mass column density was kept the same in every input model. The depth index equals 0 at the top of the chromosphere and increases downward through the chromosphere and the photosphere. The line formation regions were determined from the maximum values of the contribution to the line profile. *Lower left and right:* The height of the chromosphere as a function of mass column density and temperature. The height was calculated assuming a R=70$R_\odot$ radius. The Hα core forms between depths 16-21 (8000−9900 K, depending on T_{max}); the wings form between depths 24-35 (5800−7800 K, depending on T_{max}). See Section 3 for more information.

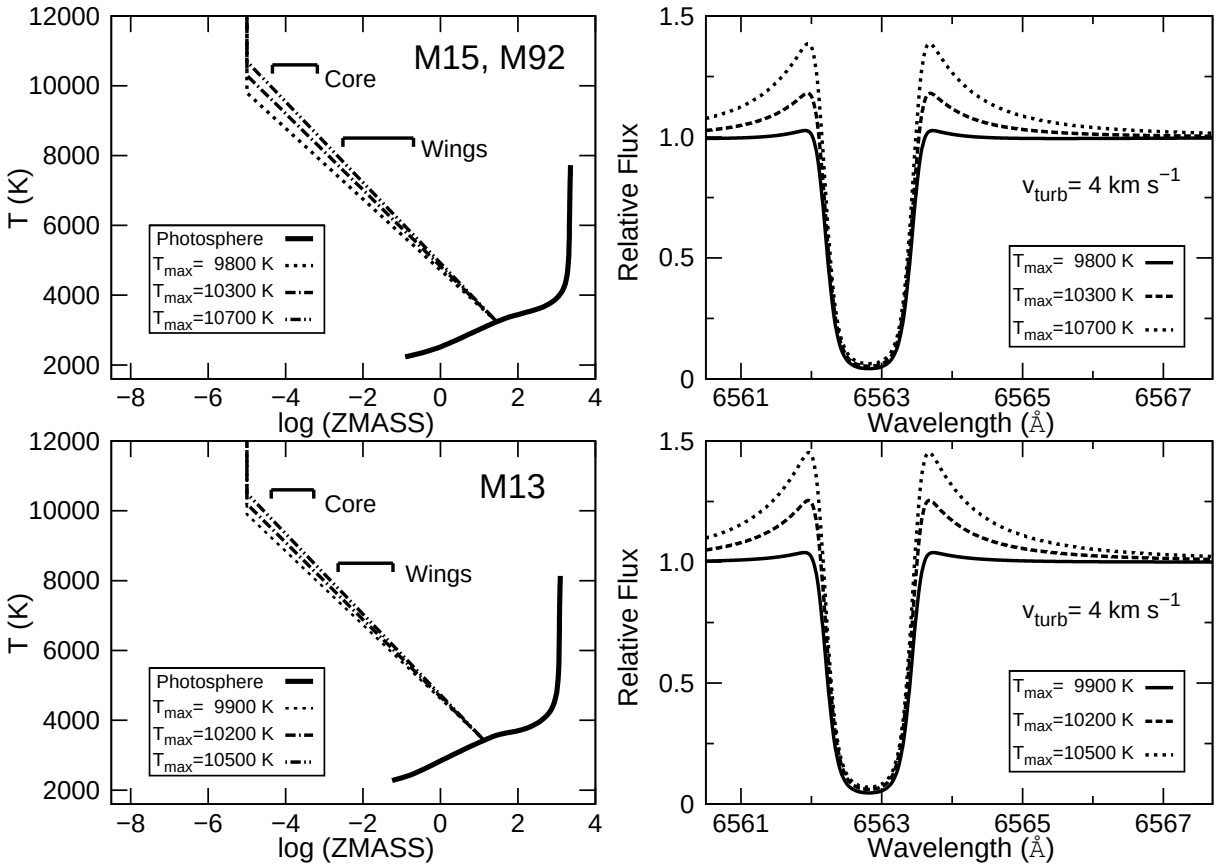

Fig. 3.— *Top left:* The temperature distribution of the chromosphere as a function of mass column density for three of the input models for M15 and M92. The solid line is the Kurucz model without any chromosphere. In all cases the chromosphere extends to ZMASS=1×10^{-5} (g cm^{-2}), where the transition region starts. T_{max} is the maximum temperature of the chromosphere. The regions of formation for the Hα wing and core are marked. *Top right:* Hα profiles for 3 models. Only a few hundred K differences in the maximum temperature result in large changes in the emission. The three static input models use 4 km s^{-1} for the turbulent velocity, constant with depth. *Lower panels:* The same results for the models of stars in M13.

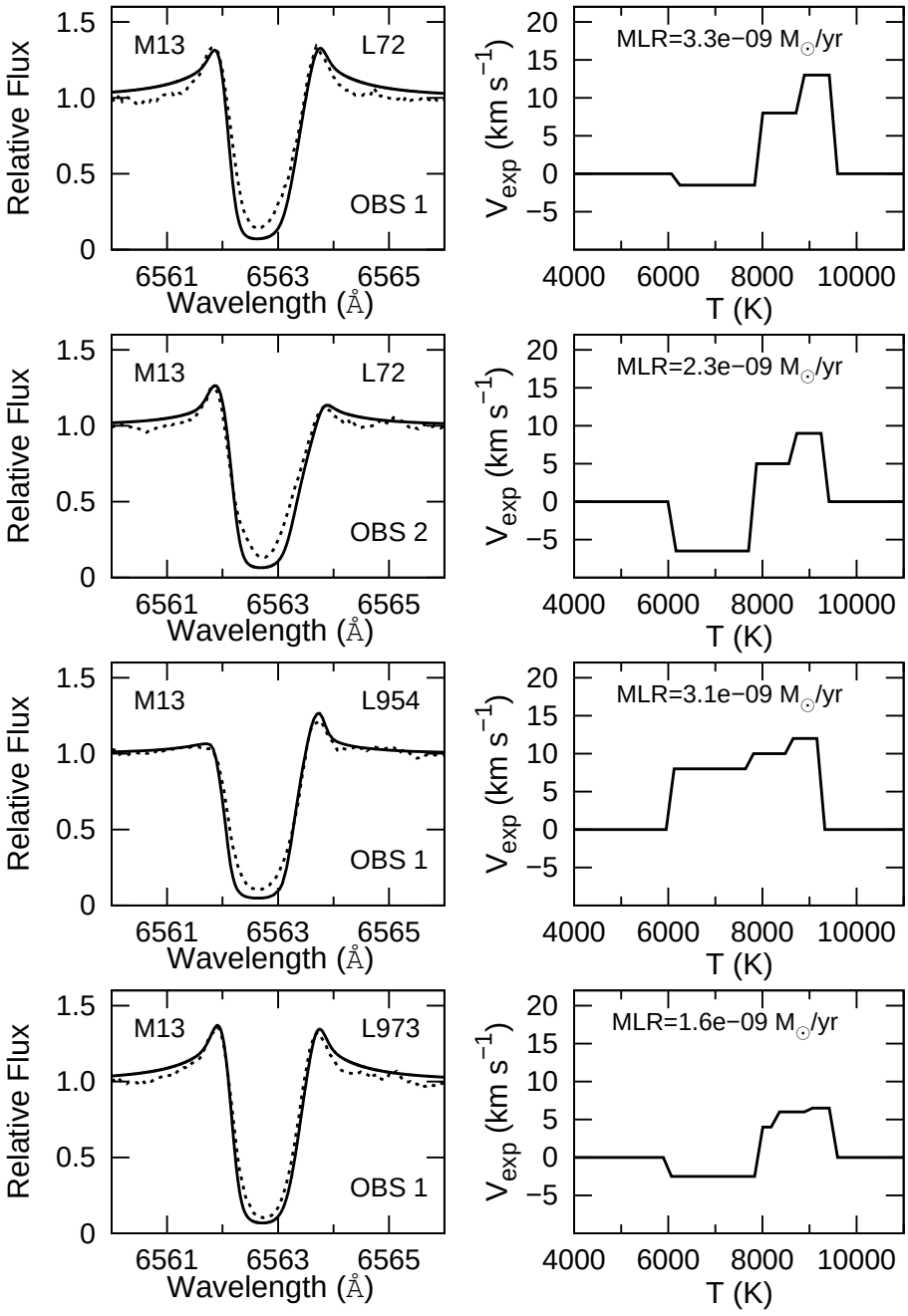

Fig. 4.— *Left panels*: Calculated spectra compared to the observations of stars in M13. The solid line shows the calculated line profile; the broken line marks the observation. *Right panels:* The expansion velocity (v_{exp}) used to match the line profile as a function of temperature. The expansion velocity is positive for a outwardly moving flow and negative for a inwardly moving flow. The derived mass loss rate is indicated for each model.

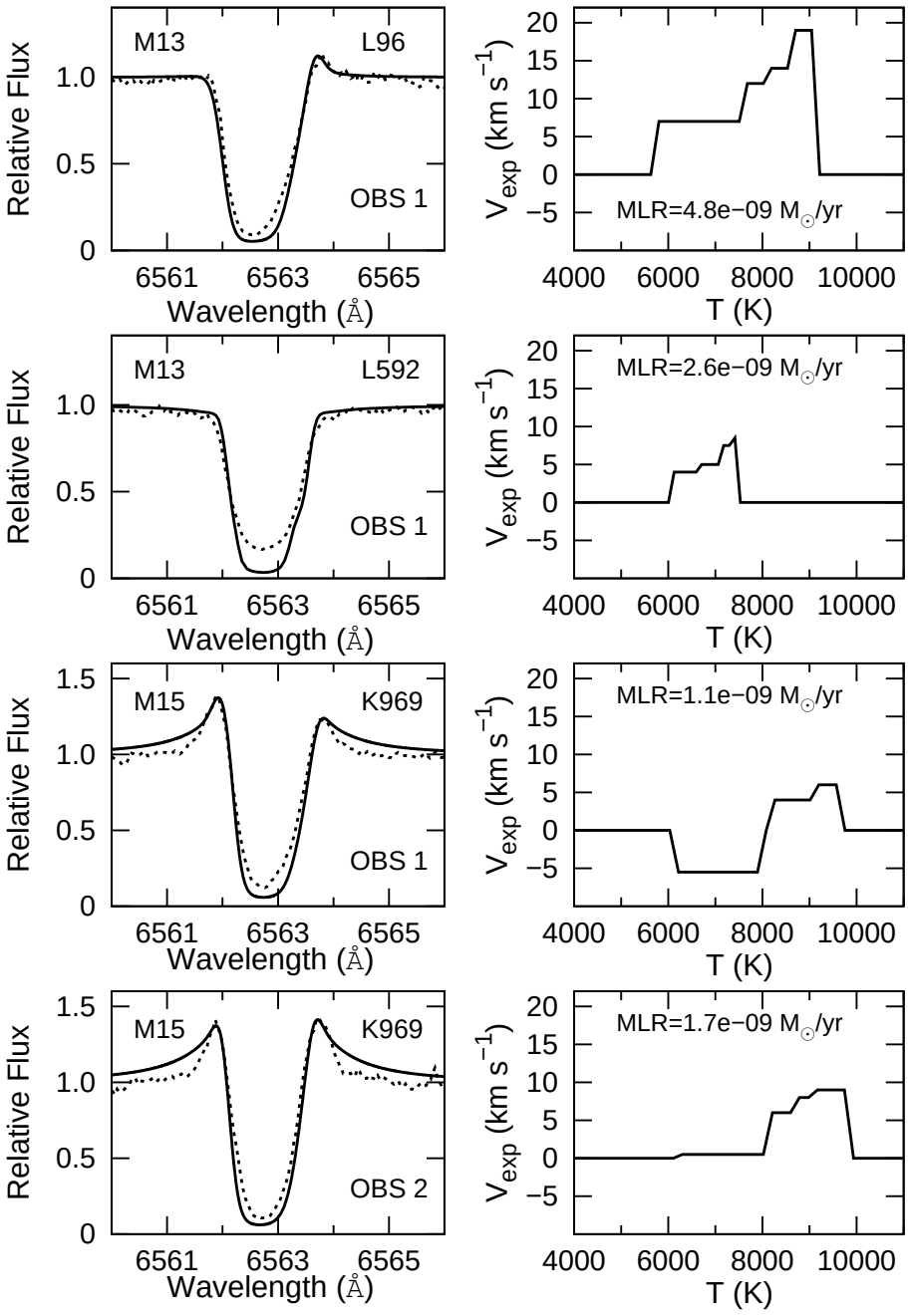

Fig. 5.— *Left panels:* Calculated spectra compared to the observations. *Right panels:* The expansion velocity used to match the line profile as a function of temperature. For additional explanation see the caption of Figure 4.

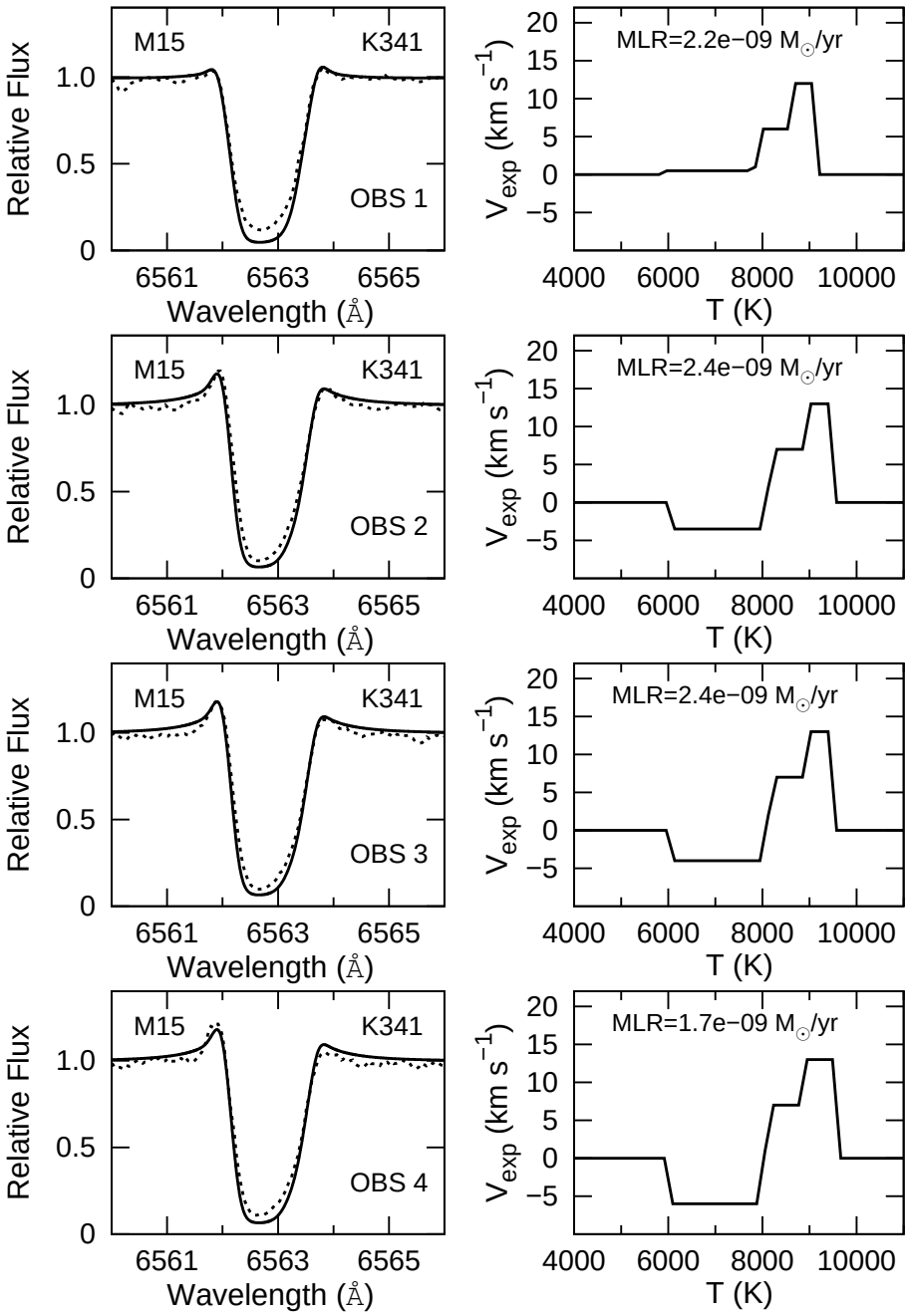

Fig. 6.— *Left panels:* Calculated spectra compared to the observations. *Right panels:* Expansion velocity used to match the line profile as a function of the temperature of the chromosphere. For additional explanation see the caption of Figure 4.

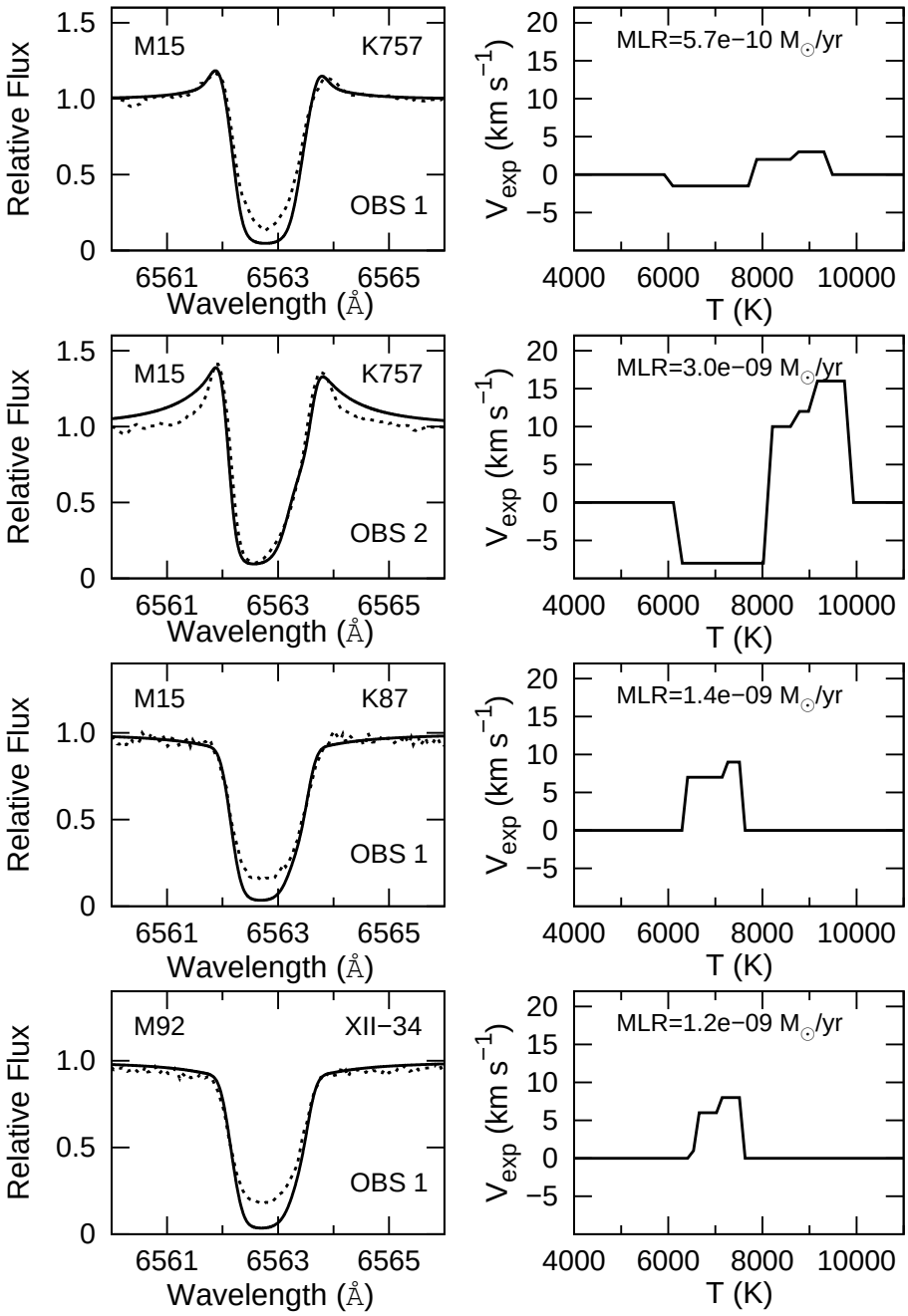

Fig. 7.— *Left panels:* Calculated spectra compared to the observations. Note the difference in the profiles between the two observations of K757. *Right panels:* Expansion velocity used to match the line profile as a function of the temperature. For additional explanation see the caption of Figure 4.

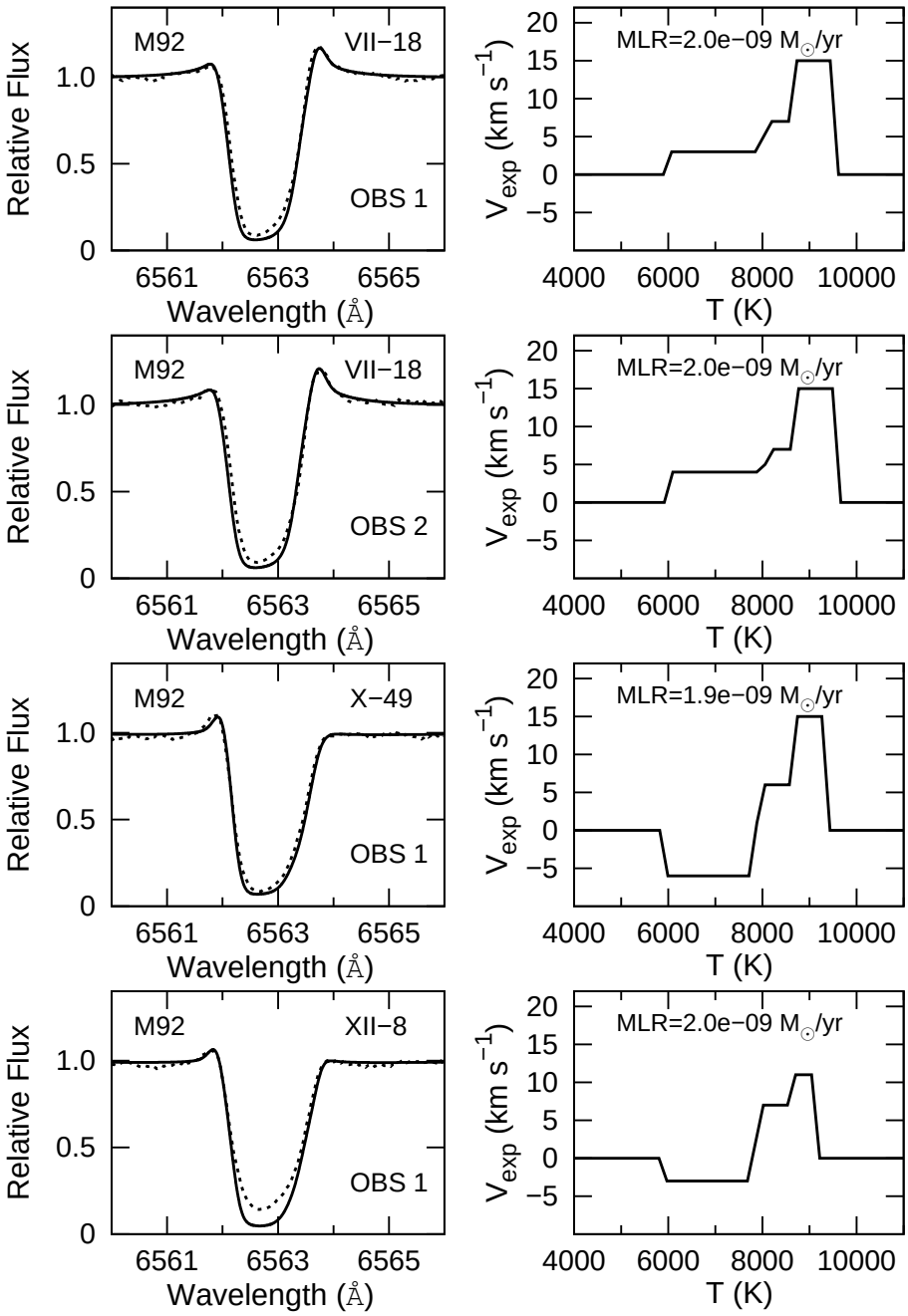

Fig. 8.— *Left panels:* Calculated spectra compared to the observations. *Right panels:* Expansion velocity used to match the line profile as a function of the temperature. Additional explanation can be found in the caption of Figure 4.

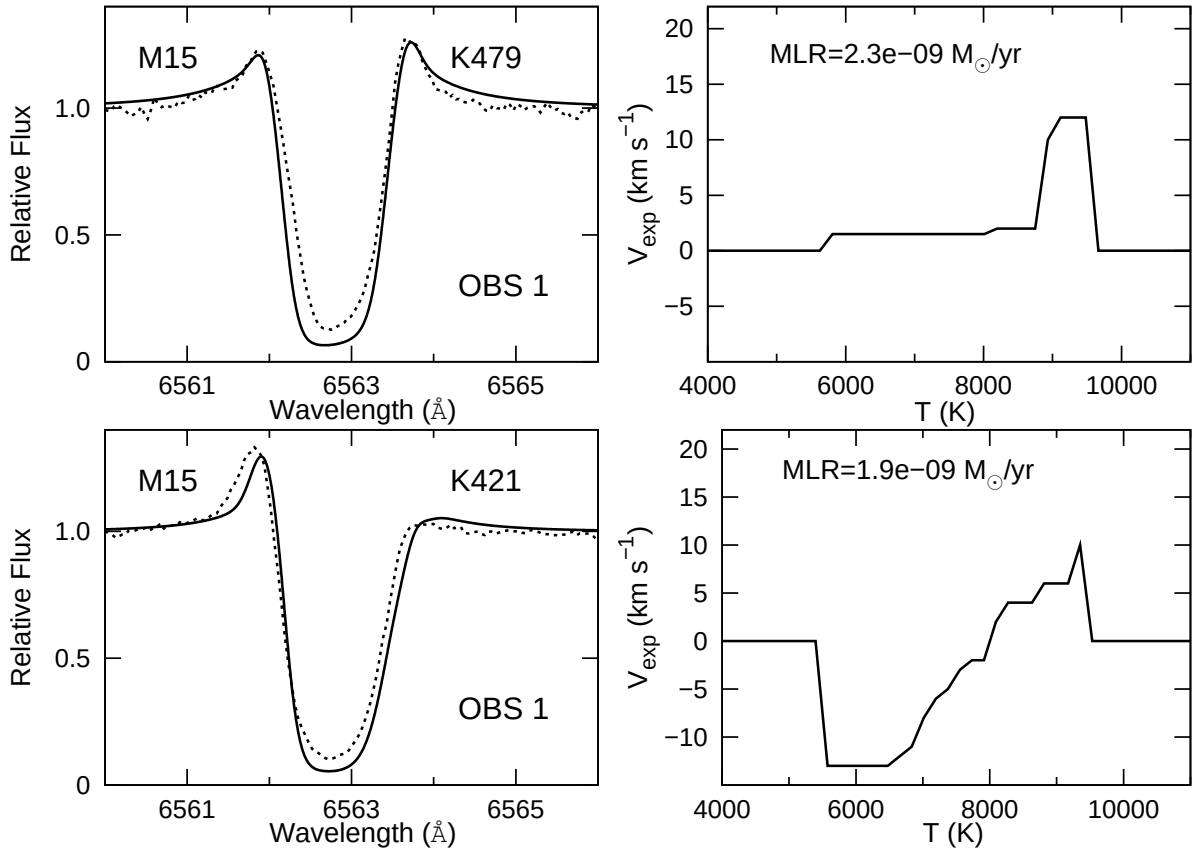

Fig. 9.— *Left panels*: Calculated spectra of giant stars identified as having circumstellar material from *Spitzer* observations (Boyer et al. 2008) compared to the observations. *Right panels:* The expansion velocity used to match the line profile as a function of temperature. Additional explanation can be found in the caption to Figure 4.

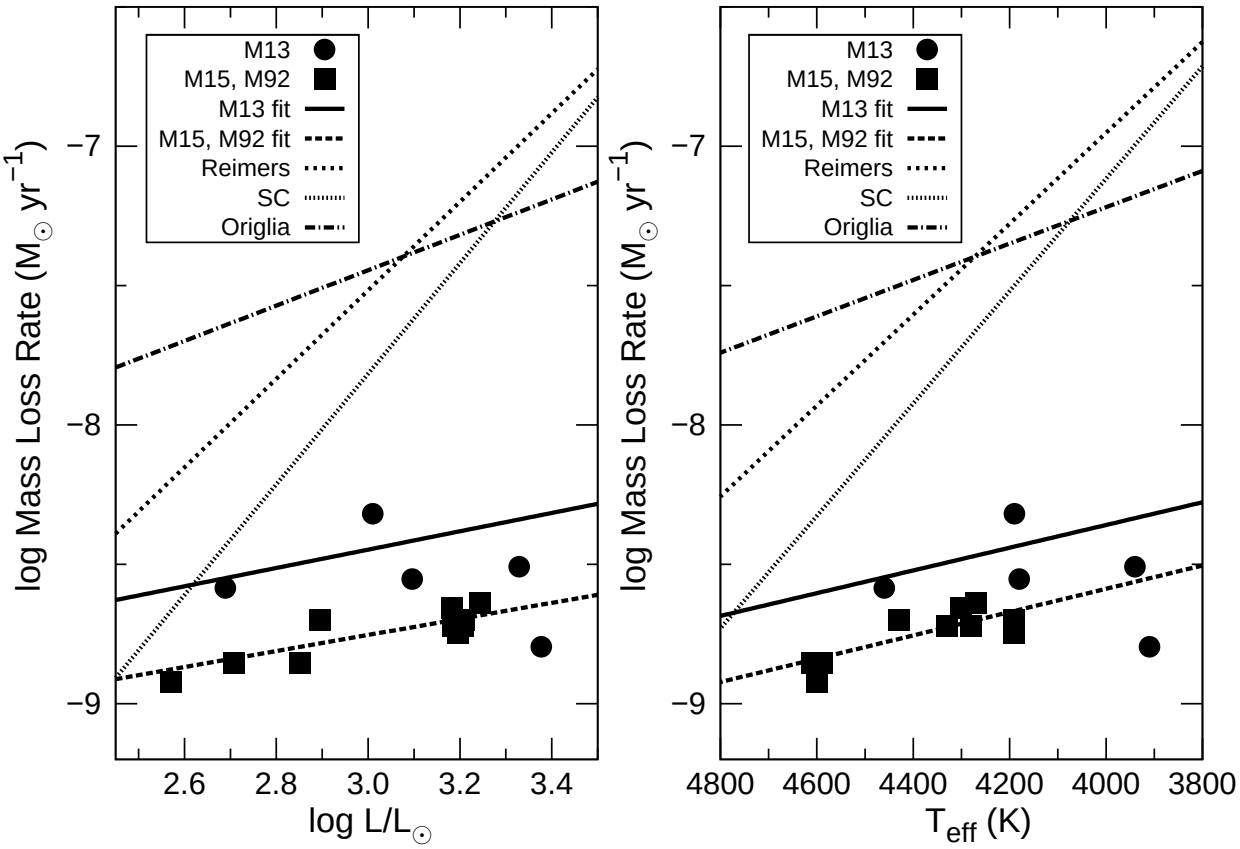

Fig. 10.— Average mass loss rates calculated in this paper (*solid circles* and *solid squares*) as compared to relations proposed by Reimers (1975, 1977), Schröder & Cuntz (2005), denoted by SC, and Origlia et al. (2007). The C parameter introduced by Origlia et al. (2007) was set equal to 1. Mass loss rates for each of the target stars were calculated from the 3 relationships, and the curves shown were fit to the individual points. Our derived mass loss rates from the Hα line profiles are almost a factor of 10 smaller than from existing mass loss approximations. The fits to the mass loss rates for M13, M15, and M92 are shown as given in Section 4.4 of the text. The two coolest stars in M13 showed small outflow velocities and were not included in the fitting procedure.

Table 1. Physical Parameters of Modeled Stars

ID No. [a]	Cluster	[Fe/H]	B−V	V	T_{eff} (K)	log $L/L_\odot$	$R/R_\odot$	log g [b] (cm s^2)
L72	M13	−1.54	1.30	12.32	4180	3.096	65.7	0.71
L96	M13	−1.54	1.27	12.52	4190	3.010	59.1	0.80
L592	M13	−1.54	1.06	13.10	4460	2.689	36.0	1.23
L954	M13	−1.54	1.54	12.09	3940	3.329	96.6	0.38
L973	M13	−1.54	1.61	12.04	3910	3.377	103.0	0.32
K87	M15	−2.26	1.07	13.80	4610	2.708	34.5	1.27
K341	M15	−2.26	1.37	12.81	4300	3.183	68.6	0.67
K421	M15	−2.26	1.20	12.72	4330	3.207	69.5	0.66
K479	M15	−2.26	1.31	12.68	4270	3.244	74.6	0.60
K757	M15	−2.26	1.43	12.88	4190	3.195	73.2	0.61
K969	M15	−2.26	1.16	13.45	4590	2.851	41.1	1.11
VII-18	M92	−2.28	1.30	12.19	4190	3.208	76.3	0.41
X-49	M92	−2.28	1.19	12.16	4280	3.184	71.2	0.48
XII-8	M92	−2.28	1.06	12.76	4430	2.896	47.7	0.83
XII-34	M92	−2.28	0.89	13.45	4660	2.570	29.6	1.24

[a]Ludendorff (1905) is the identification for stars in M13, Kustner (1921) is the identification for stars in M15, and Sandage & Walker (1966) is the identification for stars in M92.

[b]The gravity was calculated assuming M=0.8$M_\odot$ for each star.

Table 2. Physical Parameters of Calculated Chromospheric Models

ID No.	Obs[a] Date	T_{max} [b] (K)	$v_{bis,1}$ (km s^{-1})	v_{max} [c] (km s^{-1})	v_{esc} [d] (km s^{-1})	MLR ($M_\odot yr^{-1}$)
			M13			
L72	2	10300	-5.0 ± 0.6	13.0	54.0	3.3e-09
	5	10100	-5.7 ± 0.8	9.0	54.0	2.3e-09
L96	2	9900	-6.1 ± 0.9	19.0	57.0	4.8e-09
L592	5	8000	-2.6 ± 0.3	8.5	69.0	2.6e-09
L954	2	10000	-1.8 ± 0.6	12.0	48.0	3.1e-09
L973	2	10300	-1.9 ± 0.4	6.5	46.0	1.6e-09
			M15			
K87	8	8000	-3.9 ± 1.3	9.0	65.0	1.4e-09
K341	1	9900	-3.2 ± 0.6	12.0	51.0	2.2e-09
	6	10000	-6.9 ± 1.0	13.0	51.0	2.4e-09
	7	10300	-6.2 ± 0.6	13.0	51.0	2.4e-09
	8	10200	-6.3 ± 0.9	13.0	51.0	1.7e-09
K421	7	10250	-4.3 ± 0.7	10.0	66.0	1.9e-09
K479	8	10400	-0.7 ± 0.7	12.0	64.0	2.3e-09
K757	1	10200	-2.8 ± 0.5	3.0	50.0	5.7e-10
	6	10600	-8.9 ± 1.1	16.0	50.0	3.0e-09
K969	1	10500	-4.0 ± 0.6	6.0	57.0	1.1e-09
	8	10700	-1.7 ± 0.3	9.0	57.0	1.7e-09
			M92			
VII-18	3	10150	-3.0 ± 1.0	15.0	49.0	2.0e-09
	4	10200	-2.8 ± 0.8	15.0	49.0	2.0e-09
X-49	3	9950	-6.9 ± 0.8	15.0	50.0	1.9e-09
XII-8	3	9900	-5.6 ± 0.8	11.0	57.0	2.0e-09
XII-34	3	8000	-2.3 ± 1.3	8.0	66.0	1.2e-09

[a]Observations: 1: 2005 May 22, 2: 2006 March 14, 3: 2006 May 7, 4: 2006 May 9, 5: 2006 May 10, 6: 2006 May 11, 7: 2006 October 4, 8: 2006 October 7.

[b]The maximum mass column density of all models is 1×10^{-5} (g cm^{-2}) in the chromosphere, the stellar radius for each model is R=70$R_\odot$.

[c]The maximum expansion velocity used in the models.

[d]Escape velocity calculated at the level with the highest expansion velocity assuming M=0.8$M_\odot$.

Table 3. Mass Loss Rates (MLR) of Modeled Stars

ID No.	MLR Average ($M_\odot yr^{-1}$)	MLR Fit ($M_\odot yr^{-1}$)	MLR Reimers[a] ($M_\odot yr^{-1}$)	MLR SC[b] ($M_\odot yr^{-1}$)	MLR Origlia[c] ($M_\odot yr^{-1}$)
			M13		
L72	2.8e-09	3.8e-09	4.1e-08	2.1e-08	4.0e-08
L96	4.8e-09	3.6e-09	3.0e-08	1.4e-08	3.6e-08
L592	2.6e-09	2.8e-09	8.8e-09	3.5e-09	2.2e-08
L954	3.1e-09	4.6e-09	1.0e-07	7.1e-08	5.8e-08
L973	1.6e-09	4.8e-09	1.2e-07	9.2e-08	6.2e-08
			M15		
K87	1.4e-09	1.4e-09	8.8e-09	3.9e-09	2.2e-08
K341	2.2e-09	2.0e-09	5.2e-08	3.2e-08	4.5e-08
K421	1.9e-09	2.0e-09	5.6e-08	3.5e-08	4.6e-08
K479	2.3e-09	2.1e-09	6.5e-08	4.3e-08	4.9e-08
K757	1.8e-09	2.1e-09	5.7e-08	3.5e-08	4.6e-08
K969	1.4e-09	1.5e-09	1.5e-08	7.1e-09	2.7e-08
			M92		
VII-18	2.0e-09	2.1e-09	9.0e-08	4.8e-08	5.5e-08
X-49	1.9e-09	2.0e-09	7.8e-08	4.2e-08	5.2e-08
XII-8	2.0e-09	1.7e-09	2.7e-08	1.0e-08	3.4e-08
XII-34	1.2e-09	1.4e-09	7.9e-09	2.5e-09	2.1e-08

[a]Rate from Reimers (1975, 1977).

[b]Rate from Schröder & Cuntz (2005).

[c]Rate from Origlia et al. (2007).